

# Hydrate Nucleation in Water Nanodroplets: Key Factors and Molecular Mechanisms

Lei Wang, Zhengcai Zhang, and Peter G. Kusalik\*

Cite This: *Energy Fuels* 2023, 37, 1044–1056

Read Online

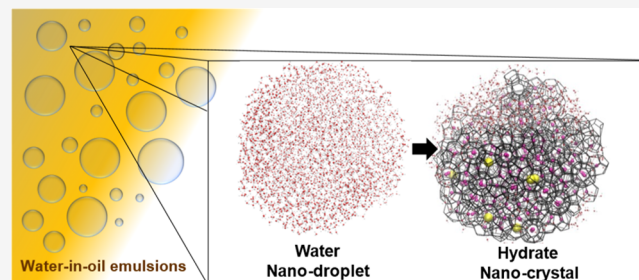
ACCESS |

Metrics &amp; More

Article Recommendations

Supporting Information

**ABSTRACT:** Clathrate hydrate nucleation in heterogeneous systems, such as the water-in-oil emulsions found in pipeline environments, is of considerable technological importance and scientific interest. While there has been a number of experimental studies investigating hydrate nucleation in water-in-oil emulsions, there have been essentially no molecular simulations to provide important molecular insights into the hydrate nucleation process. Here, we report extensive molecular dynamics simulations of gas hydrate nucleation to examine nucleation behavior in water nanodroplets immersed in a non-aqueous liquid, probing key factors impacting nucleation, including guest species, guest compositions, size of the nanodroplets, and temperature. The nucleation behavior with pure-guest (i.e., H<sub>2</sub>S, C<sub>3</sub>H<sub>8</sub>, and CO<sub>2</sub>) and H<sub>2</sub>S-containing mixtures, where the second guest species is one of C<sub>3</sub>H<sub>8</sub>, CH<sub>4</sub>, C<sub>2</sub>H<sub>6</sub>, and CO<sub>2</sub>, has been studied. For the various systems examined in this study, we find that H<sub>2</sub>S always tends to initiate hydrate formation, with the only exception being the H<sub>2</sub>S/CO<sub>2</sub> mixture, where the relatively high solubility of H<sub>2</sub>S compared to the other guest species is identified as an important factor for the current systems. Three different sizes of water nanodroplets at different temperatures are used to examine hydrate nucleation with pure-H<sub>2</sub>S guest systems, where the observed mechanism of hydrate nucleation within nanodroplets exhibits behavior similar to that found in bulk counterparts. Within water nanodroplets, the hydrate nucleation process features the initial formation of amorphous solids, which can then be annealed into more recognizable hydrate-like structures. Detailed cage analyses provide insights into the impacts of temperature and the size of the water nanodroplet on the initial location and the induction time of hydrate nucleation. Our simulations improve the understanding of the molecular mechanism of clathrate hydrate nucleation in water-in-oil emulsions, thus helping the development of hydrate-related applications and exploitation.



## INTRODUCTION

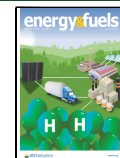
Clathrate hydrates are crystalline inclusion compounds where guest species are enclathrated in hydrogen-bonded water cages. The interest in clathrate hydrates has increased significantly in recent years because of their considerable scientific and industrial importance.<sup>1–5</sup> The vast global deposits of natural gas hydrate reservoirs, representing the most abundantly available resource of methane, have been considered as a promising clean energy resource to balance the global energy demand and reduce greenhouse gas emissions.<sup>1,2,4,5</sup> Innovative hydrate-based applications,<sup>4,6</sup> such as CO<sub>2</sub> sequestration, H<sub>2</sub> storage, gas separation, seawater desalination, and wastewater treatment, have drawn tremendous attention and have been appraised as important practical techniques for sustainable development.<sup>6</sup> Meanwhile, the undesirable hydrate-associated blockages in oil/gas pipelines or the reformation of gas hydrates during exploitation are key flow assurance issues that can seriously damage equipment and represent major safety hazards. As a consequence, it is of significant importance to understand the molecular mechanisms of the nucleation of gas hydrates to offer improved means to control the formation of clathrate hydrates.

Given the stochastic nature of nucleation and the very small time and length scales (nanoseconds and nanometers) involved, even state-of-art experimental measurements have formidable challenges to get access to the early stages of nucleation. Supporting experiments, molecular dynamics (MD) simulations have been an excellent tool, which can capture deeper insights into the molecular mechanisms of nucleation. An impressive body of MD studies has been devoted to the investigation of mechanisms of hydrate nucleation in various conditions.<sup>7–34</sup> These conditions include bulk homogeneous aqueous solutions<sup>7,15,16,26,30</sup> or heterogeneous conditions, where a bulk aqueous solution is in contact with an external surface or molecules,<sup>10,19,21–23,31,34</sup> is in contact with a guest species phase,<sup>8,19,21,22</sup> has an immersed

Received: November 2, 2022

Revised: December 19, 2022

Published: January 4, 2023



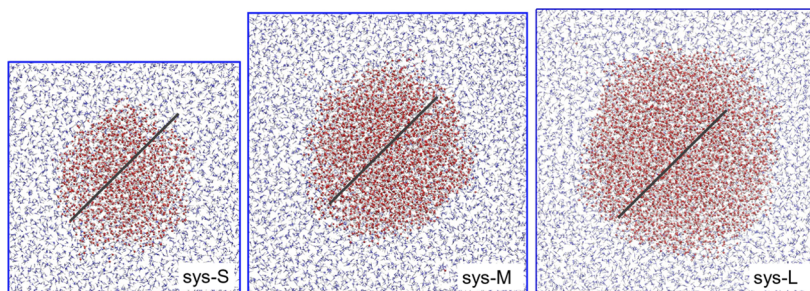


**Figure 1.** Representative initial configurations for different sizes of systems examined in this study. Water molecules are shown by red spheres (oxygen) and white spheres (hydrogen), and the guest molecules ( $\text{H}_2\text{S}$  species) are displayed by blue lines. A 5.0 nm scale bar represented by the black solid line is shown in each system to aid the eye.

guest species bubble,<sup>7,11,17,20,24–28</sup> or is within porous media confined conditions.<sup>9,12,18,29,32–34</sup> While various conditions have been explored by MD studies, to the best of our knowledge, the mechanisms of the hydrate nucleation within small water droplets immersed in a non-aqueous liquid have not yet been investigated. The condition of water droplets immersed in a non-aqueous liquid can be seen as a reasonable physical analogue of water-in-oil emulsions and for studying the nucleation mechanisms of gas hydrates therein. It is also worth noting that in many of the previous cases, owing to computational costs, simulations have been performed under highly supersaturated conditions of guest species (relative to the respective equilibrium aqueous solution) that are not typically comparable to experimental saturation conditions.

Numerous experimental studies have focused on the nucleation behavior of hydrate formation within water-in-oil emulsions, as the key component of multiphase pipelines in oil/gas production.<sup>36,37</sup> Factors such as the size of water droplets, temperatures, waxes, asphaltenes, and nanoparticles, which may impact hydrate nucleation behavior within water-in-oil emulsions, have been studied.<sup>36–54</sup> However, hydrate nucleation mechanisms in water-in-oil emulsions are still unclear. Although not the first study, one influential work on hydrate nucleation in water-in-oil emulsions is that of Turner,<sup>36</sup> in which he proposes a shell model for hydrate formation where hydrate nuclei initially form and then grow at the water droplet surface. This shell model of hydrate formation in water-in-oil emulsions is supported by the results of Aichele et al.<sup>50</sup> and Haber et al.<sup>51</sup> However, in small dispersed water droplets exposed to the gas phase, Moudrakovski et al.<sup>55</sup> explored  $\text{CH}_4$  and  $\text{CO}_2$  hydrate formation via  $^1\text{H}$  magnetic resonance microimaging and found that the hydrate typically prefers growing as small crystals in the bulk region rather than generating a shell at the edge of the water droplet. The impacts of the water cut (volume fraction of the fluid mixture) and temperature on the induction time of  $\text{CO}_2$  hydrate formation in water-in-oil emulsions have been studied by Zheng et al.<sup>42</sup> In accordance with the shell model, they proposed that the hydrate nucleation initially occurred at the interface of water-in-oil emulsions and the induction time decreased with the decrease in the size of the water droplet as well as with reduced temperature because of a higher driving force and a larger temperature gradient for heat removal at a lower temperature.<sup>42</sup> Crude oil types and different methods of hydrate preparation resulting in different hydrate structures (sII or sI) in water-in-oil emulsions saturated with methane were examined by Stoporev et al.<sup>44</sup> They claimed that the content

(e.g., C<sub>2</sub>–C<sub>4</sub> hydrocarbons) in the oil, the water cut, and thermodynamics conditions may contribute to the formation of the metastable sII methane hydrate.<sup>44</sup> Following up this work, they found that decreases in temperature<sup>45</sup> and decreases in the size of aged water droplets<sup>46</sup> can facilitate  $\text{CH}_4$  hydrate nucleation in water-in-oil emulsions. Although a great number of experimental studies associated with clathrate hydrate nucleation in water droplets have been reported, these studies have provided only indirect information about nucleation behavior, and molecular mechanisms of gas hydrate nucleation in water droplets remain unclear. Studies focus on nucleation in confinement (e.g., the natural occurrence environment of gas hydrates<sup>56</sup> and hydrate nucleation in porous media<sup>57</sup>), where the stability of the hydrate phase is strongly influenced by melting temperatures, is also related and will benefit from an improved understanding of mechanisms of gas hydrate nucleation in water nanodroplets.

Thus, in the current study, the nucleation mechanisms of gas hydrates in water nanodroplets have been studied. How guest species, guest composition, the size of the water nanodroplet and temperature may impact hydrate nucleation behavior in water nanodroplets are explored. Three different sizes of water nanodroplets immersed in a non-aqueous (guest species) liquid were generated for the study (as shown in Figure 1). There are three primary advantages of the current system setup: a realistic saturation of guest species in the water nanodroplets, a free boundary condition provided by the nanodroplet for gas hydrate formation and annealing, and a large reservoir of guest molecules provided by the non-aqueous guest species liquid. The exploration of nucleation via MD simulations focused on the pure guest species, specifically  $\text{H}_2\text{S}$ ,  $\text{C}_3\text{H}_8$ , and  $\text{CO}_2$ , and various  $\text{H}_2\text{S}$ -containing mixtures, where the second guest species is one of  $\text{C}_3\text{H}_8$ ,  $\text{CH}_4$ ,  $\text{C}_2\text{H}_6$ , and  $\text{CO}_2$ . In the simulations of pure-guest systems, nucleation events were only observed with  $\text{H}_2\text{S}$ , while in those of mixed-guest systems, the majority of hydrate cages detected were occupied by  $\text{H}_2\text{S}$ , except for  $\text{H}_2\text{S}/\text{CO}_2$  mixtures, where the slightly higher solubility of  $\text{CO}_2$  in the nanodroplet results in the number of cages occupied by both guest molecules being comparable. As  $\text{H}_2\text{S}$  is primarily involved in forming hydrate cages, we probe the molecular-level nucleation behavior in detail with systems for pure- $\text{H}_2\text{S}$  guests. The hydrate nucleation mechanisms in water nanodroplets, consistent with the observations in bulk aqueous solutions, involve the initial formation of amorphous structures which can be further annealed into more crystalline solids at elevated temperatures. Through detailed cage analyses, we find that, in general, elevating the temperature and decreasing the size of the water

nanodroplet can induce a preferred tendency of the nucleus to initially appear near the center of water nanodroplets. The induction time required for nucleation is also impacted by the temperature and the size of the water nanodroplet. Additionally, the guest solubility reduction and melting point depression arising from the decreased size of the nanodroplet are also examined.

## METHODS

**System Preparation for Nucleation.** To explore clathrate hydrate nucleation in water nanodroplets, systems with a water nanodroplet immersed in a non-aqueous liquid were employed. In this study, three different sizes of systems (labelled as sys-S, sys-M, and sys-L) were considered, which consist of 1500, 3000, and 4500 water molecules and 6000, 10 000, and 10 000 guest molecules, respectively (see Figure 1). Following a 10 ns initial equilibration at 290 K and 10 MPa, the system was then sequentially quenched in steps of 10 to 260 K, where the simulation time for each temperature was typically 10 ns. For pure-H<sub>2</sub>S systems, 10 independent production trajectories were then generated at 260, 255, and 250 K, where the production runs ranged from 400 to 600 ns, depending on the time needed to see hydrate nucleation. For studying nucleation behavior with other pure guests (C<sub>3</sub>H<sub>8</sub> or CO<sub>2</sub>) and with H<sub>2</sub>S-containing mixtures, where the other guest species is one of CH<sub>4</sub>, C<sub>2</sub>H<sub>6</sub>, C<sub>3</sub>H<sub>8</sub>, and CO<sub>2</sub>, sys-M systems were employed and the same system preparation procedures as for the pure-H<sub>2</sub>S systems were used, where further details are given in the Supporting Information.

**System Preparation for Dissociation.** The system preparation for dissociation is detailed here for H<sub>2</sub>S-occupied sI hydrate nanocrystallites, where a similar approach is used for the other crystallites of interest. A spherical nano-crystallite with the designated number of H<sub>2</sub>O molecules (e.g., 4500 for sys-L) was cut from a bulk sI clathrate hydrate crystal with all cages singly occupied by H<sub>2</sub>S guests. This spherical crystallite was then immersed into liquid H<sub>2</sub>S to build the initial configuration for the determination of the melting temperature. To measure the melting temperature, the configuration was first equilibrated at 260 K and 10 MPa for 2 ns with restrained positions of all H<sub>2</sub>O molecules. Then, the melting temperature of the nanocrystallite was determined by repeatedly increasing the temperature, initially in steps of 5 or 10 K with simulations of 15, 30, and 40 ns for sys-S, sys-M, and sys-L, respectively. When close to the melting temperature (i.e., within 5 K), sets of 10 independent simulations were run in steps of 1 K, and the melting temperature was then identified as that temperature for which at least half of the trajectories were observed to have melted. Consequently, we estimate that the error bar associated with the melting temperature is  $\pm 1$  K. To determine the disappearance of the hydrate crystal and hence its melting temperature, the potential energy, along with the number of complete cages (CCs) in the largest cage cluster, was utilized. The hydrate crystallites were labeled as melted when a significant increase of the potential energy as a function of time occurred; such trajectories consistently ended up with fewer than 4 CCs in the largest cage cluster.

**Computational Details of Simulations and the Analyses.** Throughout this study, the following methodological details were used for all simulations unless stated otherwise. Direct MD simulations were carried out using the GROMACS package.<sup>58</sup> The equations of motion were integrated using the leap-frog algorithm with a 2 fs time step. For the Lennard-Jones potentials, a cut-off of 1.2 nm was used, and the cross terms were determined using Lorentz-Berthelot,<sup>59</sup> except for the interactions between CO<sub>2</sub> and H<sub>2</sub>O. Between CO<sub>2</sub> and H<sub>2</sub>O, two strategies for the cross-terms of the Lennard-Jones interactions were considered (detailed in the Supporting Information). In brief, the first, referred to as CO<sub>2</sub><sup>v</sup>, was proposed by Míguez et al.<sup>60</sup> and accurately reproduces the phase coexistence line (hydrate-liquid H<sub>2</sub>O-liquid CO<sub>2</sub>) up to 200 MPa, while overestimating the solubility of CO<sub>2</sub> in H<sub>2</sub>O. The other, referred to as CO<sub>2</sub><sup>s</sup>, was proposed by Costandy et al.<sup>61</sup> and has been shown to

provide a good description of the solubility of CO<sub>2</sub> in H<sub>2</sub>O, yet it underestimates the phase coexistence temperatures. For the electrostatic interactions, smooth particle mesh Ewald (PME)<sup>62</sup> was used with a 1.2 nm cut-off for the real space.

Water was modeled using the TIP4P/Ice potential,<sup>63</sup> and H<sub>2</sub>S was simulated with a four-site model proposed by Forester et al.<sup>64</sup> with the H-S bond set to 0.134 nm. All molecular models are rigid in this study. The model parameters for all species have been widely used in hydrate-related studies,<sup>13,15,19,25–27,30,65–71</sup> and more details are provided in Table S1. The temperature was controlled using a Nosé-Hoover thermostat with a time constant of 2.0 ps,<sup>72</sup> and the pressure was controlled using an isotropic Parrinello-Rahman barostat with a time constant of 4.0 ps.<sup>73</sup> All simulations used periodic boundary conditions in all three dimensions. Most of simulations reported in this paper are under NPT conditions at a pressure of 10 MPa, where values other than 10 MPa will be explicitly provided otherwise. Under these conditions and for the models employed in the study, H<sub>2</sub>S,<sup>64,74</sup> CO<sub>2</sub>,<sup>75,76</sup> C<sub>2</sub>H<sub>6</sub>, and C<sub>3</sub>H<sub>8</sub> are in the liquid phase (see Figure S1), while CH<sub>4</sub> is a supercritical fluid.<sup>77,78</sup>

To monitor trajectories for nucleation events, the F<sub>4</sub> order parameter, a four-body order parameter based on the torsion angle of two adjacent water molecules, was utilized.<sup>79</sup> The average F<sub>4</sub> value is 0.7 for both sI and sII hydrates and -0.04 for liquid water.<sup>80</sup> Given that a water cluster in the non-aqueous liquid with more than 3 adjacent molecules is a very rare event, the average F<sub>4</sub> value measured in our systems reasonably describes the phase conversion in the water nanodroplet. The specific cage structures and corresponding occupancies were analyzed by a modified version of FSICA [face-saturated incomplete cage (IC) method].<sup>81</sup> Briefly, the cages detected by FSICA can be grouped into two categories: CCs, where all vertices are connected by at least 3 edges, and ICs. The standard (std) cages (i.e., 5<sup>12</sup>6<sup>n</sup>-4<sup>1</sup>5<sup>10</sup>6<sup>m</sup>, where n = 0, 2, 3, and 4 and m = 2, 3, and 4), which are also CCs, have been identified and monitored because of their significant roles in the hydrate formation process in previous studies.<sup>9,11,13,17,25,70,82–85</sup> Other cages that are not std cages are labeled as non-standard (non-std) cages. We note that 5<sup>12</sup> and 5<sup>12</sup>6<sup>2</sup> cages are the cage components of the unit cell of the sI hydrate structure, and 5<sup>12</sup> and 5<sup>12</sup>6<sup>4</sup> cages are the cage components of the unit cell of the sII hydrate structure.

For the structure analyses, 10 ps intervals were used for collecting the data, and all results for the time evolution of structures reported in this study are 1 ns rolling averages of the data sets unless stated otherwise. We note that empty std cages and multi-occupancy cages are rare events in the systems explored and so were not included in the analysis unless stated otherwise. All initial configurations in this study were built using the PACKMOL package,<sup>86</sup> and all configurations were visualized with VMD.<sup>87</sup>

## RESULTS AND DISCUSSION

**Solubility within Water Nanodroplets.** Since the nucleation events observed in this study involved H<sub>2</sub>S-filled cages almost exclusively, and since nucleation has a strong dependence on the guest concentration,<sup>30,33,65,89</sup> we initiate our investigation by measuring the concentration of H<sub>2</sub>S in the water nanodroplets. We note that for the current systems where a water nanodroplet is immersed in a non-aqueous liquid, the two phases (water/non-aqueous liquid) are in compositional equilibrium; thus, the concentrations of the guest species in the aqueous solution are essentially their saturated values, which represent their solubilities.

The solubility of guest species in the nanodroplet was determined from 100 ns MD simulations performed at 280 K for the systems of interest, where the final 50 ns trajectory was used for analysis. The boundaries of the core region of nanodroplets were then identified by the plateaus in the density profiles (e.g., as seen in Figure S2 and presented in Figure S4A). The cut-offs of the radii, defining the core regions

of the water nanodroplets, are 1.5, 2, and 2.5 nm for sys-S, sys-M, and sys-L, respectively. The solubilities were then determined from the integration of radial density profiles for H<sub>2</sub>O and H<sub>2</sub>S over the core regions. The solubilities of other guest species of interest were measured in the same way. As presented in Table S2, we find that the solubility of H<sub>2</sub>S slightly decreases as the size of the nanodroplet decreases. The solubility of C<sub>3</sub>H<sub>8</sub> in the nanodroplets, which is around 2 orders of magnitude lower than that of H<sub>2</sub>S in the bulk water phase,<sup>90,91</sup> was also measured (see Figures S3 and S4 and Table S2). The solubility reduction for C<sub>3</sub>H<sub>8</sub> with decreasing size of the nanodroplet is a relatively large effect. This somewhat unexpected decrease in the solubility of these guest species with decreasing nanodroplet size can be partially explained from a simple thermodynamic basis (as detailed in Supporting Information). Further work aimed at investigating this reduction of the solubility in water nanodroplets should be undertaken but is beyond the scope of the present study.

**Melting Points of Hydrate Nanocrystals.** The influence of local environments on the stability of hydrate phases,<sup>88</sup> for example, the melting point depression of confined hydrates,<sup>12,29,92</sup> and of spherical hydrate particles<sup>14,93</sup> has been previously identified. The size-dependent melting points for H<sub>2</sub>S-filled SI hydrate nano-crystallites are also of interest in this study. When spherical hydrate nano-crystallites are introduced into a non-aqueous liquid (e.g., H<sub>2</sub>S), some melting of the surface, for example, of ICs on its boundary, can be expected. This surface liquid layer will coat the crystalline hydrate core.<sup>94,95</sup> Thus, the determination of the size of the nanocrystallite is not straightforward. If we define an upper bound ( $R_{\max}$ ) of the radius for the crystalline nanoparticle as the edge of the plateau in the radial density profile of H<sub>2</sub>O molecules prior to any melting of the nanoparticles (i.e., its structural edge), and define a lower bound ( $R_{\min}$ ) of the crystalline nanoparticle as the cut-off of the core of the respective water nanodroplet (see Table S2), then the effective radius,  $R$ , of the crystalline nanoparticle should be in the range of ( $R_{\min}$ ,  $R_{\max}$ ). If we assume a water/liquid H<sub>2</sub>S interface thickness of 0.8 nm and take  $R$  to be at the midpoint of the interface, then  $R$  is equal to  $R_{\max}$  minus 0.4 nm. Such values of  $R$  are essentially an average of  $R_{\max}$  and  $R_{\min}$ .

The dependence of melting temperatures on  $R$  for the nanoparticle, as presented in Table 1 and Figure 2, is well expressed by the Gibbs–Thomson (G–T) equation<sup>96,97</sup>

$$T_m(R) = T_m^{\text{bulk}} - \frac{2K_{\text{GT}}}{R} \quad (1A)$$

and

$$K_{\text{GT}} = \frac{T_m^{\text{bulk}} \gamma \nu}{\Delta H_m} \quad (1B)$$

where  $T_m^{\text{bulk}}$  is the melting point of the bulk phase of the crystalline hydrate,  $\gamma$  is the solid–liquid surface tension,  $\nu$  is the molar volume (the value of which is detailed in Supporting Information), and  $\Delta H_m$  is the bulk enthalpy for melting. From

**Table 1. Sizes and Melting Points of Pure-H<sub>2</sub>S Systems**

system	melting point (K)	$R_{\min}$ , $R_{\max}$ (nm)	$R$ (nm)
sys-L	291.0 ± 1	2.5, 3.3	2.9
sys-M	287.5 ± 1	2.0, 2.8	2.4
sys-S	279.0 ± 1	1.5, 2.2	1.8

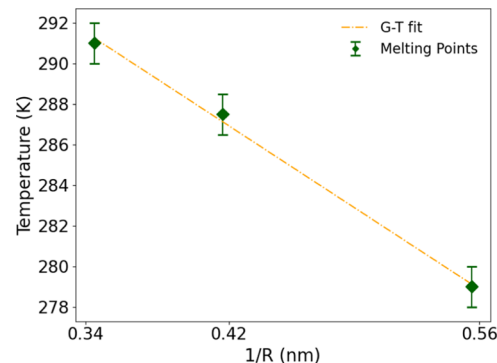


**Figure 2.** Melting temperatures of H<sub>2</sub>S-occupied sI nanocrystals as a function of 1/R, where R is the radius of the nanoparticle. The yellow dashed line is the fit of the Gibbs–Thomson equation (eqs 1A and 1B).

the fit of the G–T equation, we obtain the  $T_m^{\text{bulk}}$  of 311.1 K for the H<sub>2</sub>S-occupied sI crystal and  $K_{\text{GT}}$  of 28.8 K·nm. The value of  $T_m^{\text{bulk}}$  is in good agreement with the value of 315 K obtained for a bulk H<sub>2</sub>S hydrate sI.<sup>26</sup> We note that the  $T_m^{\text{bulk}}$  predicted is about 10 K higher than the experimental value of 303 K.<sup>98</sup> Using  $\Delta H_m = 6.5$  kJ/mole of water,<sup>14,63</sup> we can obtain an interfacial tension,  $\gamma$ , of H<sub>2</sub>S-sI crystallite/liquid H<sub>2</sub>S of 31.6 mJ/m<sup>2</sup> from eq 1B. To the best of our knowledge, there are no reports of experimental values for these conditions. We can, however, compare to results from other studies with similar systems. These include interfacial tension values of 36 mJ/m<sup>2</sup> for the CH<sub>4</sub> and CO<sub>2</sub> hydrate particle/water interface<sup>14</sup> and 64.28 mJ/m<sup>2</sup> for the CH<sub>4</sub>/C<sub>3</sub>H<sub>8</sub> mixed hydrate/hydrocarbon interface<sup>93</sup> as well as surface tensions in the range of 28–32 mJ/m<sup>2</sup> for the CH<sub>4</sub> and CO<sub>2</sub> hydrate–solution interface determined from experimental measurements with porous media.<sup>56,99</sup> Thus, our result is in line with previously reported values.

Utilizing the same methodology (detailed in Methods) for sys-M systems, we estimate a melting point of 274 ± 1 K for a C<sub>3</sub>H<sub>8</sub>-occupied sII hydrate nanoparticle, where only large cages are occupied, and a melting point of 309 ± 1 K of a H<sub>2</sub>S/C<sub>3</sub>H<sub>8</sub>-occupied sII hydrate nanoparticle, in which H<sub>2</sub>S occupies the small cages (S<sup>12</sup>) and C<sub>3</sub>H<sub>8</sub> occupies the large cages (S<sup>12</sup>6<sup>4</sup>). Inspecting the melting points from the three different guest-occupied hydrate nanoparticles, the melting temperature of the H<sub>2</sub>S-occupied sI particle is located in between that of the C<sub>3</sub>H<sub>8</sub>-occupied and of H<sub>2</sub>S/C<sub>3</sub>H<sub>8</sub>-occupied sII hydrate nanoparticles. With all S<sup>12</sup> cages empty in the C<sub>3</sub>H<sub>8</sub>-occupied sII nanoparticle, the crystalline structure is apparently less stable, as expected.

**Nucleation Process.** Of the guest species studied, H<sub>2</sub>S was consistently found to dominate the hydrate nuclei in water nanodroplets for both pure-guest and mixed-guest systems (see Tables S3–S6 and Figures S6–S11). Thus, our examination of nucleation behavior will primarily focus on the H<sub>2</sub>S-containing systems. For pure-H<sub>2</sub>S guest systems, three different sizes of water nanodroplets at three different temperatures have been employed to elucidate the impact of the size of the water nanodroplets on the hydrate nucleation behavior.

Given the stochastic nature of nucleation, it is important to average over several trajectories to obtain estimates of the average behavior for comparison. The relative time strategy,<sup>24,26,85,100</sup> which has been demonstrated to provide excellent temporal alignment for nucleation events, particularly

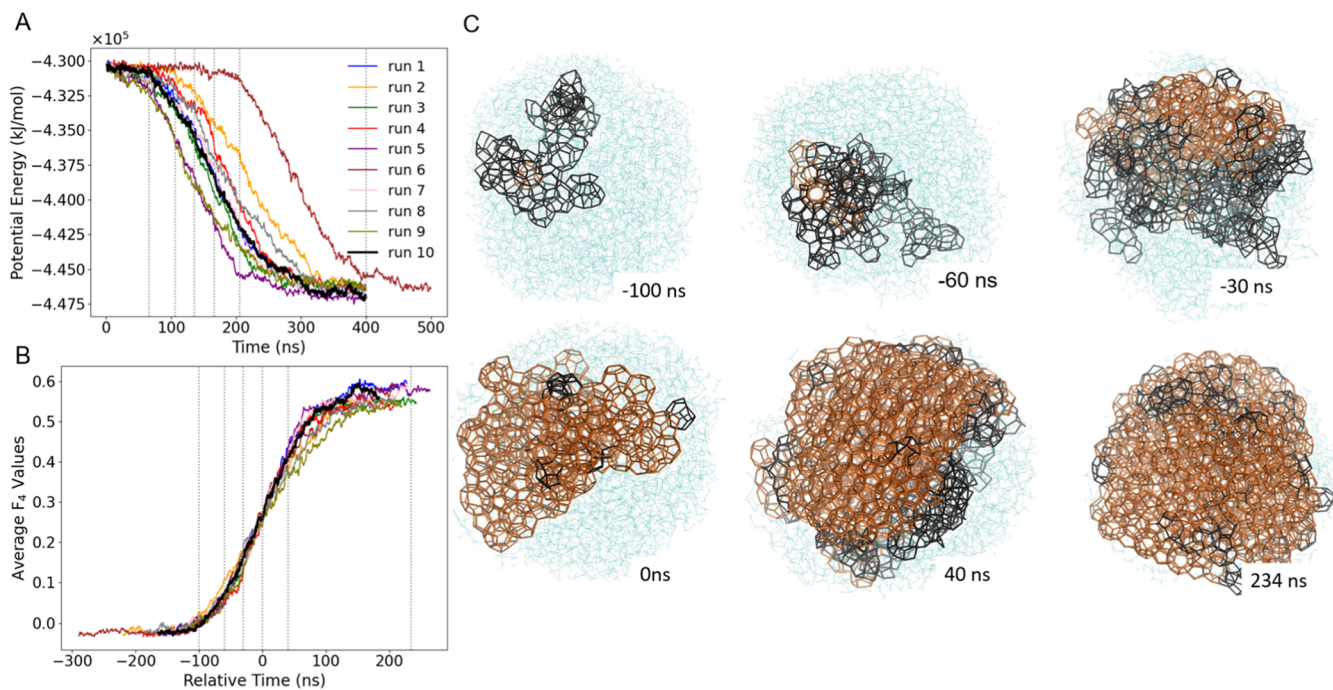


**Figure 3.** Hydrate nucleation process of pure-H<sub>2</sub>S systems for sys-L at 250 K. (A) Time evolution of the potential energy for each run. (B) Evolution of the average  $F_4$  values for all nucleating trajectories. The relative time scale, which yields temporally aligned curves, is used. Panels (A,B) use the same color pattern. (C) Snapshots of the largest cluster taken at various stages of the nucleation process from a representative trajectory, run 10, highlighted by a heavy black line in panels (A,B). Std cages are shown as orange tubes, and non-std cages are displayed as black tubes. The liquid water molecules are shown by cyan lines. The H<sub>2</sub>S molecules in cages, in the aqueous and non-aqueous liquid phases, are omitted for visual clarity. The time index provided in panel (C) is the relative time. The dashed lines in panels (A,B) correspond to the time points of the snapshots shown in panel (C).

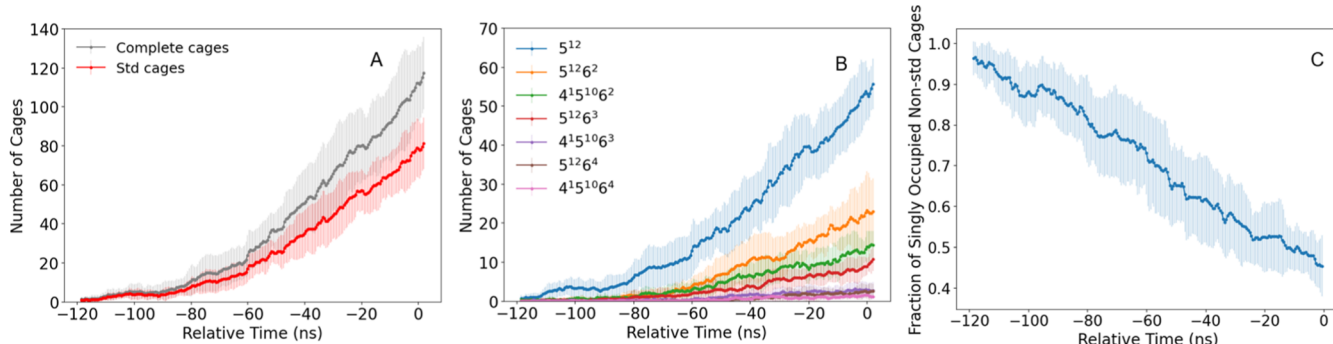


**Figure 4.** Evolution of cages of pure-H<sub>2</sub>S systems for sys-L at 250 K as a function of the relative time: (A) complete and std cages; (B) most-probable std cages; (C) fraction of singly occupied non-std cages. The error bars representing the standard deviations are included.

for the early stage of nucleation, is utilized in the current study for comparing nucleation events across different conditions. Briefly, the relative time scale ( $t_{\text{relative}}$ ) is obtained by subtracting the time corresponding to the inflection point of a sigmoidal function fitted to the average  $F_4$  values from the real time for a specific nucleating trajectory. Thus,  $t_{\text{relative}} = 0$  ns is the time point with the maximum rate of hydrate ordering (as measured by the change in  $F_4$  values) in the system; hence, nucleation occurs at  $t_{\text{relative}} < 0$  ns. While we can see in Figure 3A that hydrate nucleation occurs at different times for pure-H<sub>2</sub>S systems, in Figure 3B, the  $F_4$  curves representing the conversion of the liquid to the hydrate phase in the systems exhibit excellent overlap. From Figure 4A,B, we can see the appearance of cages consistent with the increase of the  $F_4$  values, signaling the onset of the transition to the hydrate

phase. The early stage of nucleation is of particular interest in this study, and thus,  $t_{\text{relative}} < 0$  ns will be our primary focus.

The nucleation process for sys-L with a pure-H<sub>2</sub>S guest at 250 K is presented in Figure 3. We note that the other systems and different temperatures we have investigated show similar nucleation behavior. As shown in Figure 3A,B, the appearance of the nucleus corresponds with a decrease in the potential energy and an increase in the average  $F_4$  values. The successive snapshots of the system configurations from a typical trajectory, run 10, which are the black curves in Figure 3A,B, are presented in Figure 3C. At  $t_{\text{relative}} = -100$  ns, the appearance of the largest cluster with a  $5^{12}$  cage surrounded by several non-std cages is observed in agreement with the high percentage of the singly occupied non-std cages, as seen in Figure 4C. As the nucleation proceeds, the hydrate nucleus begins to grow with a core primarily of std cages (in orange)

surrounded by non-std cages (in black) (see Figure 3C), until  $t_{\text{relative}} = 0$  when the majority of cages comprising the largest cluster are std cages. At the end of the simulation, almost the entire water nanodroplet has transformed into a hydrate cluster, leaving only a few non-std cages and a small number of liquid-like  $\text{H}_2\text{O}$  molecules on its surface. Notably, the nucleation behavior observed within systems and different temperatures, consistent with previous work,<sup>1,7,8,25,27,66</sup> supports a two-step mechanism for hydrate nucleation in which the conversions from the aqueous phase to the hydrate phase go through intermediate amorphous structures in which standard cages of the solid yet lack long-ranged order (e.g., see the snapshot of the configuration at  $t_{\text{relative}} = 234$  ns in Figure 3C). Moreover, these intermediate amorphous structures appear to arise from more disordered structures, for example, the predominant guest-occupied non-std cages in Figures 3C, S6–S8B, and S10B, or the “blob” precursors,<sup>8</sup> rather than directly from the aqueous solution.

To examine further the impact of different guest species on nucleation in nanodroplets, extensive sets of MD simulations were performed within sys-M containing pure  $\text{C}_3\text{H}_8$  or  $\text{CO}_2$  guest species, with multiple runs each up to 600 ns (see Table S4). For the  $\text{C}_3\text{H}_8$  systems, there are no nucleation events observed over a total simulation time of 3  $\mu\text{s}$  even at a lower temperature of 245 K. This is apparently due to the rather low solubility of  $\text{C}_3\text{H}_8$  in the water nanodroplet, as presented in Table S2, as well as the fact that  $\text{C}_3\text{H}_8$  can only fit into the large (e.g.,  $5^{12}6^4$ ) cages. For the  $\text{CO}_2$  systems, even with  $\text{CO}_2^v$ , for which the solubility is elevated and slightly higher than that of the current  $\text{H}_2\text{S}$  model (see Table S2), nucleation is not observed to occur on the current simulation timescale of 2  $\mu\text{s}$ . This observation can be partially explained by the behavior previously noted in the literature where the concentration of  $\text{CO}_2$  is still below the critical concentration necessary for  $\text{CO}_2$  hydrate nucleation to occur.<sup>30,82</sup> Additionally,  $\text{CO}_2$  molecules prefer to form  $4^{15}10^{6^2}$  cages to accommodate the shape of  $\text{CO}_2$  molecules,<sup>82</sup> but these cages have a higher entropic penalty associated with their formation compared with the  $5^{12}$  cage.<sup>85</sup>

Since for pure-guest systems nucleation events have been only observed with  $\text{H}_2\text{S}$ , our study of the mixed hydrate nucleation behavior will focus on  $\text{H}_2\text{S}$ -containing guest mixtures, where the other species is one of  $\text{C}_3\text{H}_8$ ,  $\text{CH}_4$ ,  $\text{C}_2\text{H}_6$ ,  $\text{CO}_2^v$ , or  $\text{CO}_2^s$  with a guest ratio of 50/50 for sys-M (see Table S5). One of the most interesting aspects of the nucleation behavior observed from these mixed systems and their dependence upon different guest mixtures is that the initial hydrate nucleus that forms consistently has almost all cages filled by  $\text{H}_2\text{S}$  molecules and only rarely occupied by the other guest species (e.g., as shown in Figures S6–S10). The only exception to this is for  $\text{H}_2\text{S}/\text{CO}_2$  mixed systems, where the relatively high solubility for  $\text{CO}_2$  in the water nanodroplet is apparently the key factor (noting that  $\text{C}_3\text{H}_8$ ,  $\text{CH}_4$ , and  $\text{C}_2\text{H}_6$  have low solubilities in water). During nucleation of  $\text{H}_2\text{S}/\text{CO}_2$  mixed systems with the same guest compositions,  $\text{CO}_2$  and  $\text{H}_2\text{S}$  show distinct preferences for specific cage types, as shown in Figure S11, where  $\text{H}_2\text{S}$  molecules tend to occupy the smaller (i.e.,  $5^{12}$ ) cages, while  $\text{CO}_2$  molecules favor the larger (i.e.,  $4^{15}10^{6^2}$ ) cages. This behavior, consistent with previous works,<sup>26,82,84</sup> is more pronounced for the  $\text{CO}_2^v$ -modeled systems (see Figure S11) and is attributed to the higher solubility of this  $\text{CO}_2$  model in water.

Meanwhile, we further note that, as shown in Table S6 and Figure S10, cages associated with hydrate nucleation are still  $\text{H}_2\text{S}$  predominantly occupied even with a higher ratio of  $\text{C}_3\text{H}_8$  in  $\text{H}_2\text{S}/\text{C}_3\text{H}_8$  mixed systems. Additionally, according to the radial density profiles for the mixed systems (e.g., as shown in Figure S5), the peak in the density profile for  $\text{H}_2\text{S}$  always lies on the non-aqueous liquid side near the interface, indicating the accumulation of  $\text{H}_2\text{S}$  molecules at the interface. This accumulation of  $\text{H}_2\text{S}$ , apparently acting as a surfactant, is analogous to the elevated density of  $\text{CO}_2$  at the interface of a  $\text{CO}_2/\text{CH}_4$  mixture in water (see Figure 3 in ref 101).

Previous MD studies of hydrate nucleation with  $\text{H}_2\text{S}/\text{CH}_4$  guest mixtures in bulk aqueous solutions<sup>26</sup> revealed that with comparable initial concentrations for both guest species in the aqueous solutions, the numbers of singly occupied cages for the two guests are also similar. Additionally, these results also indicate that  $\text{H}_2\text{S}$ -filled cages are kinetically favored, particularly at low temperatures, and  $\text{CH}_4$ -filled cages are stabilized by elevated temperatures. To further examine the impact of the water nanodroplet condition on cage occupancy for  $\text{H}_2\text{S}/\text{CH}_4$  guest mixtures, nucleating runs were also performed at a pressure of 20 MPa (see Table S5), where the final configurations were then used for annealing simulations of 250 ns at 270 K and 20 MPa. We again emphasize here that under the current conditions, where the concentrations for the guests in aqueous nanodroplets are determined by their solubilities, the dissolution of  $\text{CH}_4$  or other light hydrocarbons are relatively rare events. For example, the concentration of  $\text{H}_2\text{S}$  in the core region of the water nanodroplet is roughly an order of magnitude higher than that of  $\text{CH}_4$ . These initial concentrations for the guest species result in a cage occupancy ratio of around 10 in favor of  $\text{H}_2\text{S}$ , as presented in Figure S9. As apparent in Figure S9, an increase in the pressure somewhat increases the relative percentage of  $\text{CH}_4$  occupancy. If the initial (amorphous) hydrate nucleus formed at 250 K and 20 MPa is now warmed and allowed to anneal, we find that the  $\text{CH}_4$  occupancy shows a small but definitive increase, suggesting that, if giving sufficient time, this crystallite would achieve the appropriate equilibration occupancy for  $\text{CH}_4$  in cages. More details about the annealing of the mixture hydrate structure will be discussed below.

Given that  $\text{H}_2\text{S}$  is the guest species that is primarily responsible for the initial hydrate cage formation in the current conditions, our further detailed analyses of nucleation mechanisms will focus on pure- $\text{H}_2\text{S}$  guest systems. The quantitative analysis of the cage formation, as shown in Figure 4 for sys-L at 250 K, is consistent with previous studies focusing on the formation of gas hydrates in bulk aqueous solutions.<sup>11,13,25,26,66,67,85</sup> For std cages, in good agreement with previous studies,<sup>13,25,26,66,67,85</sup>  $5^{12}$  cages usually appear first and tend to predominate the std-cage population, followed by  $5^{12}6^2$ , then  $4^{15}10^{6^2}$ ,  $5^{12}6^3$ , and  $4^{15}10^{6^3}$  cage, with  $5^{12}6^4$  and  $4^{15}10^{6^4}$  cages being rare. Moreover, as apparent in Figure 4, other CC cages also form (see panel A), as the formation of the nucleus proceeds, and singly occupied non-std cages initially predominate in the system but then decrease in proportion.<sup>25,26,85</sup> Similar observations of cage populations and proportions were observed in the other systems and conditions explored. It has been previously conjectured that non-std cages tend to form initially since they are kinetically favored but will then undergo specific cage transitions into the std cages that are the components of hydrate crystalline structures (such as sI structures).<sup>26,102</sup> We note that final structures formed in the

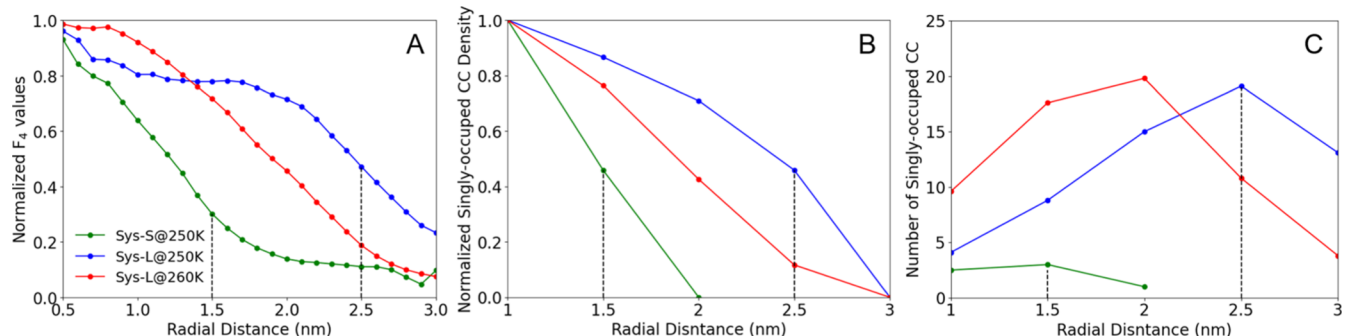


**Figure 5.** Radial profiles of order parameters from the nanodroplet center at  $t_{\text{relative}} = -30 \text{ ns}$ : (A) for average  $F_4$  values; (B) for singly occupied CC density [i.e., the number of cages per volume ( $\text{nm}^3$ )]; (C) for the number of the singly occupied CC. The same color scheme is applied in all panels for sys-S at 250 K (sys-S@250 K), sys-L at 250 K (sys-L@250 K), and sys-L at 260 K (sys-L@260 K). The  $F_4$  values were averaged over 2 ns for each nucleating trajectory within a 0.1 nm thick spherical shell, then averaged over all nucleating trajectories. The density and number of CCs were averaged over all nucleating trajectories. The normalized values in panels (A,B) were obtained by min–max feature scaling. In panels (B,C), the distances provided are the upper radii of the 0.5 nm thick spherical shells. The boundaries of the cores of the nanodroplets ( $R = 1.5 \text{ nm}$  for sys-S,  $R = 2.5 \text{ nm}$  for sys-L) are represented by the black dashed lines.

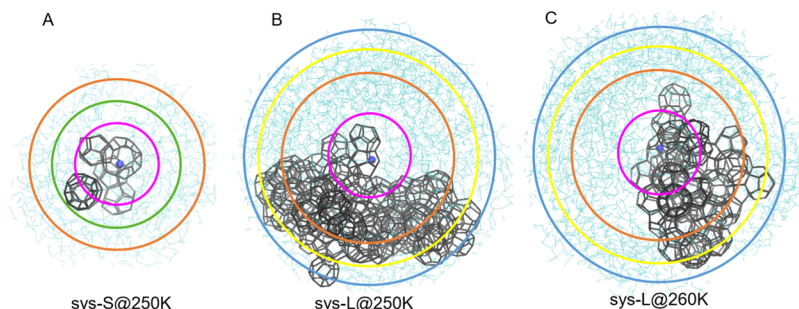


**Figure 6.** Representative configurations showing the location of the nuclei comprising all singly occupied CCs for different systems: (A) sys-S at 250 K (sys-S@250 K) taken from run 2 at 176 ns; (B) sys-L at 250 K (sys-L@250 K) taken from run 10 (the black curves in Figure 2A,B) at 136 ns; (C) sys-L at 260 K (sys-L@260 K) taken from run 10 at 443 ns. The singly occupied CCs are connected by black tubes. The liquid water molecules are shown as cyan lines. The  $\text{H}_2\text{S}$  molecules in cages, in the aqueous, and in the non-aqueous liquid phases are omitted for visual clarity. The colored circles are to aid the eye, where radii of 1.0, 1.5, 2.0, 2.5, and 3.0 nm are displayed by magenta, green, yellow, brown, and blue heavy lines, respectively.

present simulations of water nanodroplets are dominated by std cages (e.g., see Figure 3C) exhibiting good short-ranged order yet essentially lacking long-ranged order. We will discuss this point further below.

**Location of the Nuclei.** For the current systems, a water nanodroplet immersed in a non-aqueous liquid is saturated with the guest species; that is to say, the aqueous solution making up the nanodroplet is in compositional equilibrium with the surrounding non-aqueous liquid. The formation of hydrate nuclei and where they tend to appear should depend on both the ability of the guest species to diffuse into the water nanodroplet and the ability of the guest molecules to promote cage formation. Again, focusing primarily on pure- $\text{H}_2\text{S}$  systems, the water/liquid  $\text{H}_2\text{S}$  interface may intuitively be considered as a potential locale for the embryonic development of the nuclei given its easy access to both additional water and  $\text{H}_2\text{S}$  species. If correct, then one would expect a hydrate shell to form readily at the interface, which would then hinder the further mass transfer of the guest molecules needed for the further growth of the hydrate. The majority of experimental results for the formation of hydrate indicate such behavior, where an unconverted water core is inside a hydrate shell,<sup>36,50,51</sup> and the nucleation rate has been found to depend on a water/oil surface area within the water-in-oil emulsion.<sup>35,37</sup> However, here we report that at the nanoscale the hydrate nucleation behavior in water nanodroplets can be more complex.

To elucidate the size and temperature dependences of the preferred location for the initial formation of the hydrate nuclei, the radial profiles for (1) average  $F_4$  values,  $F_4(R)$ ; (2) singly occupied CC density,  $\rho_{\text{CC}}(R)$ ; and (3) the number of singly occupied CC have been generated to identify the location of hydrate formation at a variety of stages during the nucleation process (i.e.,  $t_{\text{relative}} = -100, -50, -30, \text{ and } 0 \text{ ns}$ ) for different systems and temperatures (see Figures S12–S14). In Figure 5, representative results at  $t_{\text{relative}} = -30 \text{ ns}$  are presented comparing the locations of nuclei for sys-S at 250 K, sys-L at 250 K, and sys-L at 260 K. As indicated by the steeper curves approaching the center of the nanodroplet in Figure 5A, the  $F_4(R)$  profile implies, on average, a shift of the preferred site of the nuclei toward the center of the nanodroplet by decreasing the size of the water droplet or elevating the temperature. In accordance with the results, the values of  $F_4(R)$  and  $\rho_{\text{CC}}(R)$  in Figure 5B also show a consistent shift of the nuclei toward the center of the nanodroplet. We can see examples as captured in Figure 6, where, with a smaller nanodroplet or at a higher temperature, the nuclei tend to reside nearer to the center of the nanodroplet.

If we, however, focus on the actual number of cages (see Figure 5C) at particular distances from the center of the nanodroplet, we observe somewhat different behavior. Specifically, we find that the apexes of the curves for the number of cages are nearer to the boundary of the core of the

nanodroplet, although also tending to shift slightly toward the center of the nanodroplet with elevated temperatures (see Figures 5C and S14). Again, examining the representative examples of locations of nuclei within these systems in Figure 6, it is clear that the volume of each spherical shell increases as  $R$  increases. Consequently, an enhanced probability of observing a hydrate nucleus form near the periphery of the nanodroplet can arise simply due to this volume effect. At the same time, we should note that the more disordered and fluctuating nature of the nanodroplet surface makes it easier for the hydrate nucleus to form within the interior of the nanodroplet. For example, for smaller systems (i.e., sys-S) where even the interface region accounts for a considerable volume, the hydrate nucleus tends to form at the center of the nanodroplet, as shown in Figure 6A, while for larger systems (i.e., sys-L), the hydrate cluster does tend to gather at the inner side of the interface rather than form shell-like solids along the interface at the current nanoscale.

With increasing the temperature, the guest diffusion rate is accelerated and thus guest molecules can more readily diffuse into the interior of the nanodroplets to counter the depletion effect during hydrate nucleation. Consequently, there is a higher likelihood that at elevated temperatures, more hydrate cages are seen forming nearer to the center of the nanodroplet, as captured in Figure 6B,C. This observation is in line with the shifting of the apexes of the number of CCs seen in Figures 5C and S14. It is important to point out that the distribution of the sizes of the water droplets generated under the experimental conditions is on the microscale,<sup>42,45,46,50,51,103</sup> which are far larger than the sizes of the water nanodroplets of the current study. Thus, in these experiments, guest species that initially diffuse into the water droplet easily can form the hydrate shell readily near the surface. The hydrate shell formed resists guest molecules' further diffusion, so an impermeable hydrate shell is formed.<sup>51</sup> However, if the size of the water droplet is confined to the nanoscale, size and temperature factors would be competitive, both of which can shift the preferred location of the initial formation of hydrate nuclei.

**Induction Time of the Nucleation.** We have also considered the impacts of the size of the nanodroplets and temperature on the induction time for hydrate nucleation. For each trajectory, the induction time for the hydrate nucleation was defined as the time when the largest persistent cluster with more than two CCs first appears.<sup>26</sup> A bar chart for the average induction times in nanodroplets of different sizes and at different temperatures is displayed in Figure 7 (detailed results are also given in Table S3). The apparent trend of the induction time indicates that, as the temperature decreases and the size of the nanodroplet increases, a shorter induction time is required for nucleation to occur. These expected trends are consistent with a larger volume of nanodroplet nucleating more quickly and a higher supercooling enhancing the nucleation rate.

**Evolution of the Crystallinity.** As noted above, the hydrate clusters observed to nucleate in systems in this study are all found to grow to eventually span the entire droplet (e.g., Figures 3C, S6–S8B, and S10B). While apparently not fully crystalline, these structures have a relatively high  $F_4$  value (around 0.6, compared to 0.7 for the hydrate crystal<sup>79</sup>), indicating a relatively complete conversion of water molecules behavior from liquid-like to solid-like. As detailed in Figure 8A,  $S^{12}$  cages are dominant in the nanoparticle structure, of which the majority are linked by sharing pentagonal faces (as shown

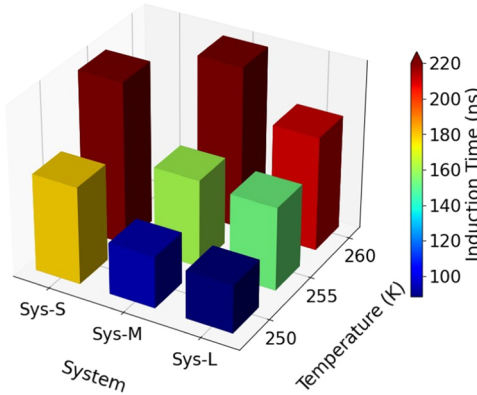


**Figure 7.** Average induction times for hydrate nucleation in different sizes of nanodroplets and at different temperatures. The red-brown bars are truncated and represent systems where nucleation is a rare event on the current simulation timescale.

in Figure 8B), a characteristic feature of the sII hydrate.  $S^{12}6^2$  cages (characteristic of the sI hydrate) have the second highest percentage, followed by  $4^15^{10}6^2$ ,  $5^{12}6^3$ ,  $S^{12}6^4$ ,  $4^15^{10}6^3$ , and  $4^15^{10}6^4$  cages. The ratio of  $S^{12}/S^{12}6^2$  in this structure is around 2, which is considerably large than the 1/3 ratio of the unit cell for the sI hydrate structure, which consists of two  $S^{12}$  cages and six  $S^{12}6^2$  cages. These cage distributions and the relatively amorphous structure of the hydrate clusters obtained in this study are otherwise very comparable to those of previous bulk-phase studies.<sup>13,25,26,66,67,85</sup> Consequently, both sI and sII motifs can be found in the incipient hydrate structure, as shown in Figure 8B.

Although amorphous nanoparticles are always observed to form initially, it is also interesting to understand how they may evolve into a more recognizable crystalline structure. In the present study, nanoparticles naturally have free boundary conditions that should allow more opportunities for restructuring relative to a typical structure formed within a bulk system simulation with periodic boundary conditions. Several final configurations were subsequently simulated at elevated temperatures to facilitate annealing. One of the successful annealing cases is shown in Figure 9. This initial amorphous nanoparticle was taken at 500 ns from run 9 of sys-M at 255 K, and we then performed a simulation with elevated temperatures, first 265 K for 100 ns, followed by 270 K for 500 ns. As apparent in Figure 9B, after a period of fluctuations, the potential energy rises briefly and then goes down before attaining a lower energy plateau, indicating that the structure has rearranged. Compared with the initial amorphous hydrate, the annealed hydrate nanoparticle, see Figure 9A, shows significantly improved crystalline order and features a dominant region with characteristics of the sI structure (blue square) and a smaller region with a sII motif (magenta square). Moreover, the ratio of  $S^{12}/S^{12}6^2$  cages, which is now close to 1 (see Figure 9C), indicates that the structure has been successfully annealed to become more sI-like. Additionally, as shown in Figure S15, we find that the nanoparticle contains only a few other non-std cages and a small number of surface liquid-like H<sub>2</sub>O molecules. To afford further insights into this annealed structure, in Figure S16 we have visualized the final structure in Figure 9B, where each image highlights a particular std cage type. From Figure S16, we can see, for example, that  $S^{12}6^3$  cages have formed and act as linking cages<sup>66,104,105</sup> in the middle of the crystalline particle, allowing the coexistence of

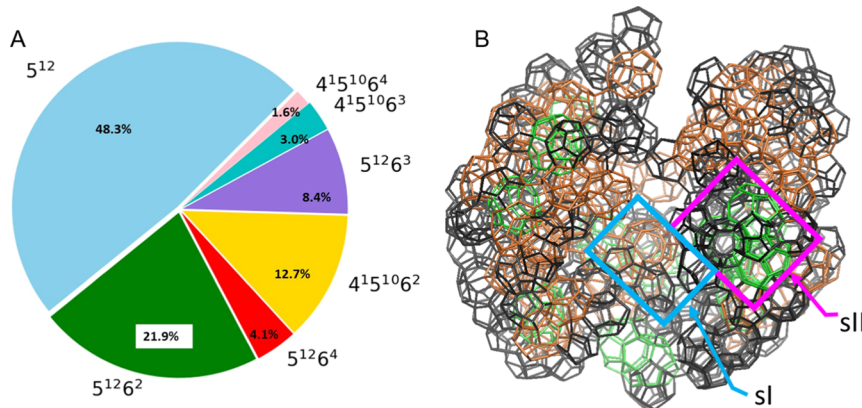


**Figure 8.** Composition of std cages for the final structures for sys-L at 250 K. (A) Percentage distribution of std cages. The results are averaged over the last 20 ns from all nucleating trajectories. (B) Final hydrate structure at 400 ns for a representative trajectory, run 10 (the black curves in Figure 3A,B) in which only  $5^{12}$  (black tubes),  $5^{12}6^2$  (brown tubes), and  $5^{12}6^4$  (green tubes) cages are presented, and all other molecules are not displayed for visual clarity. Representative SI and SII motifs are highlighted with blue and magenta squares, respectively.

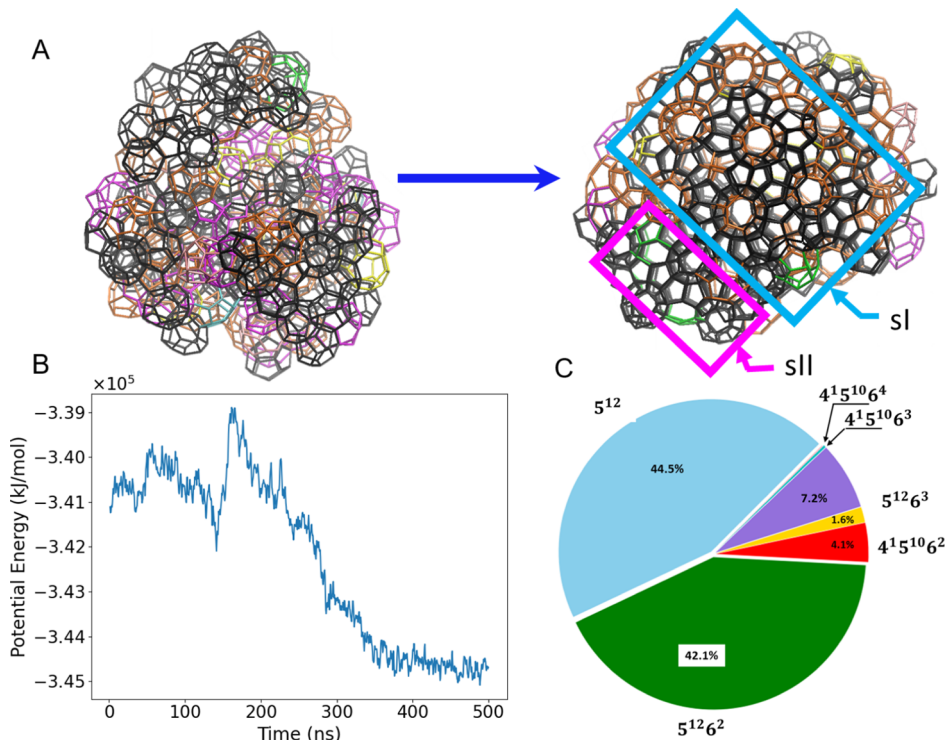


**Figure 9.** Annealing of hydrate structures. (A) Snapshot of the initial amorphous hydrate cluster taken from run 9 at 500 ns for sys-M at 255 K (left); snapshot of the final hydrate structure taken from the annealing trajectory after 400 ns at 270 K (right). In panel (A), only std cages are shown and are color-coded as black for  $5^{12}$ , orange for  $5^{12}6^2$ , green for  $5^{12}6^4$ , yellow for  $5^{12}6^3$ , magenta for  $4^{15}106^2$ , pink for  $4^{15}106^3$ , and cyan for  $4^{15}106^4$ , and all other molecules are omitted for visual clarity. (B) Time evolution of the potential energy for the annealing trajectory at 270 K. (C) Percentage distribution of std cages averaged over the last 20 ns of the annealing trajectory at 270 K.

various hydrate structural regions without any significantly higher energy penalty. Finally, we remark that a similar annealing process for the  $\text{H}_2\text{S}/\text{CH}_4$  systems with a  $\text{H}_2\text{S}$  mole fraction of 50%, as shown in Figure S9, also results in increased crystallinity of the hydrate structure as indicated by an increase in the ratio of  $5^{12}6^2$  to  $5^{12}$  cages and a decrease in the populations of other cages.

## CONCLUSIONS

Small water droplets immersed in a non-aqueous liquid are important heterogeneous hydrate formation environments, such as within water-in-oil emulsions found in gas/oil

production. Yet the hydrate nucleation mechanisms within such water droplets remain relatively unexplored at the molecular level. In this study, extensive MD simulations have been performed to study gas hydrate nucleation behavior for water nanodroplets immersed in a non-aqueous liquid for both pure-guest (specifically,  $\text{H}_2\text{S}$ ,  $\text{C}_3\text{H}_8$ ,  $\text{CO}_2$ ) systems and  $\text{H}_2\text{S}$ -containing mixed-guest systems, where the other guest species is one of  $\text{C}_3\text{H}_8$ ,  $\text{CH}_4$ ,  $\text{C}_2\text{H}_6$ , and  $\text{CO}_2$ . A notable finding of this study is that, on the current simulation timescale and for pure-guest systems, nucleation events were detected only with  $\text{H}_2\text{S}$ ; for mixed-guest systems, the initial nuclei formed always consisted of almost exclusively  $\text{H}_2\text{S}$ -occupied cages except for

H<sub>2</sub>S/CO<sub>2</sub> systems. The relative solubilities of the guest (i.e., H<sub>2</sub>S considerably higher than C<sub>3</sub>H<sub>8</sub>, CH<sub>4</sub>, and C<sub>2</sub>H<sub>6</sub> in water nanodroplets) were found to play a crucial role in determining this behavior.

A reduction of the solubility as the size of the water nanodroplet decreases has been observed. The depression of the melting temperature with decreasing size of hydrate nanocrystals was found to be well described by the Gibbs–Thomson equation, from which we extracted the sl-crystallite/liquid H<sub>2</sub>S surface tension, in agreement with other reported values. Three different systems have been examined to determine the effects of the size of water nanodroplets, along with temperature, on the hydrate nucleation behavior for pure-H<sub>2</sub>S systems. In general, we found that elevating the temperature and decreasing the size of the water nanodroplets give rise to a higher probability of density (i.e., probability per unit of volume) of the initial formation of nuclei shifting toward the center of the nanodroplet. However, if one considers only the probability, the nuclei prefer to form near the periphery of the nanodroplet as a consequence of the volume effect. At lower temperatures and within larger nanodroplets, a shorter induction time is required to observe hydrate nucleation, consistent with a higher supercooling and larger volume within which to initiate hydrate nuclei. Our results indicate that the mass transfer rate of guest species, which is impacted by temperature, could be a competitive factor in the initial formation of the hydrate nuclei within nanoscopic water droplets. However, for larger water droplets (e.g., of the microscale, the size typically seen in water-in-oil emulsions), the size of the droplets becomes the determinative factor where the formation of hydrate favors the region near the interface; thus, a hydrate shell which encloses a water core can be observed.

This study also demonstrates that gas hydrate nucleation behavior in water nanodroplets is consistent with that seen in bulk aqueous solutions, where amorphous hydrate nanoparticles form initially. During the early stages of nucleation, dominant non-std cages appear to bridge the evolution from the aqueous solution to the hydrate phase; S<sup>12</sup> cages predominate in the population of std cages. Advantaged by the free boundary of the water nanodroplets, the initial amorphous hydrate solids can be annealed into polycrystalline structures which are dominated by a sl motif.

According to the results revealed in this work, the solubility of guest species, although not a usual focus of experimental studies of hydrate nucleation in water-in-oil emulsions, has been found as a key factor for guests for rapidly initiating the formation of hydrate cages. This indicates that, with the presence of soluble guest species such as H<sub>2</sub>S, hydrates can form rapidly by initial formation of H<sub>2</sub>S-dominated hydrate nuclei and then such nuclei can transition into hydrate solids dominated by other guests. Although the complex content of oil/gas production impacts hydrate formation and aggregation in water-in-oil emulsions, the formation of a hydrate shell near the interface of the water droplets arises because of the huge interfacial area of the water-in-oil emulsion, along with the relatively low-temperature condition (2–4 °C)<sup>106</sup> involved in hydrate formation in gas/oil production. This hydrate shell formed at the interface can then hinder the mass transfer of the guest species into the water droplet. However, one needs to note that for sufficiently small water droplets, the interfacial region may no longer be preferred for hydrate formation. Thus, our results not only provide important scientific insights into

nucleation behavior in water nanodroplets; they may further facilitate the development of hydrate-based techniques and the optimization of conventional flow assurance in gas/oil production.

## ■ ASSOCIATED CONTENT

### SI Supporting Information

The Supporting Information is available free of charge at <https://pubs.acs.org/doi/10.1021/acs.energyfuels.2c03724>.

Additional details of models used, solubility and density profiles for the guest species, additional details for the Gibbs–Thomson equation, summary of simulation results for nucleation, size and temperature dependences of the preferred location of hydrate nuclei, and hydrate structures following annealing ([PDF](#))

## ■ AUTHOR INFORMATION

### Corresponding Author

Peter G. Kusalik – Department of Chemistry, University of Calgary, Calgary T2N 1N4 Alberta, Canada;  [orcid.org/0000-0001-6270-663X](https://orcid.org/0000-0001-6270-663X); Email: [pkusalik@ucalgary.ca](mailto:pkusalik@ucalgary.ca)

### Authors

Lei Wang – Department of Chemistry, University of Calgary, Calgary T2N 1N4 Alberta, Canada

Zhengcai Zhang – Laboratory for Marine Mineral Resources, Pilot National Laboratory for Marine Science and Technology, Qingdao 266071, China;  [orcid.org/0000-5945-0303](https://orcid.org/0000-5945-0303)

Complete contact information is available at: <https://pubs.acs.org/10.1021/acs.energyfuels.2c03724>

### Notes

The authors declare no competing financial interest.

## ■ ACKNOWLEDGMENTS

We are grateful for the financial support of the Natural Sciences and Engineering Research Council of Canada (RGPIN-2016-03845). We thank Compute Canada for computational resources. We also thank the Supercomputing Laboratory at IGGCAS and Center for High-Performance Computing and System Simulation, Pilot National Laboratory for Marine Science and Technology (Qingdao), for the allocation of computing time.

## ■ REFERENCES

- (1) Khurana, M.; Yin, Z.; Linga, P. A Review of Clathrate Hydrate Nucleation. *ACS Sustain. Chem. Eng.* **2017**, *5*, 11176–11203.
- (2) Yin, Z.; Linga, P. Methane Hydrates: A Future Clean Energy Resource. *Chin. J. Chem. Eng.* **2019**, *27*, 2026–2036.
- (3) Sloan, E. D.; Koh, C. A.; Koh, C. *Clathrate Hydrates of Natural Gases*; CRC Press: Boca Raton, FL, 2007.
- (4) Hassanpouryouzband, A.; Joonaki, E.; Vasheghani Farahani, M.; Takeya, S.; Ruppel, C.; Yang, J.; English, N. J.; Schicks, J. M.; Edlmann, K.; Mehrabian, H.; Aman, Z. M.; Tohidi, B. Gas Hydrates in Sustainable Chemistry. *Chem. Soc. Rev.* **2020**, *49*, 5225–5309.
- (5) Kastner, M.; Myers, M.; Koh, A. C.; Johnson, G. E.; Thurmond, J. Energy Transition and Climate Mitigation Require Increased Effort on Methane Hydrate Research. *Energy Fuels* **2022**, *36*, 2923–2926.
- (6) Dong, H.; Wang, J.; Xie, Z.; Wang, B.; Zhang, L.; Shi, Q. Potential Applications Based on the Formation and Dissociation of Gas Hydrates. *Renew. Sustain. Energy Rev.* **2021**, *143*, 110928.

- (7) Vatamanu, J.; Kusalik, P. G. Observation of Two-Step Nucleation in Methane Hydrates. *Phys. Chem. Chem. Phys.* **2010**, *12*, 15065.
- (8) Jacobson, C. L.; Hujo, W.; Molinero, V. Amorphous Precursors in the Nucleation of Clathrate Hydrates. *J. Am. Chem. Soc.* **2010**, *132*, 11806–11811.
- (9) Zhang, Z.; Kusalik, G. P.; Wu, N.; Liu, C.; Ning, F. Molecular Insights into the Impacts of Calcite Nanoparticles on Methane Hydrate Formation. *ACS Sustain. Chem. Eng.* **2022**, *10*, 11597–11605.
- (10) Zhang, Z.; Kusalik, G. P.; Guo, G.-J. Might a 2,2-Dimethylbutane Molecule Serve as a Site to Promote Gas Hydrate Nucleation? *J. Phys. Chem. C* **2019**, *123*, 20579–20586.
- (11) Walsh, M. R.; Rainey, J. D.; Lafond, P. G.; Park, D.-H.; Beckham, G. T.; Jones, M. D.; Lee, K.-H.; Koh, C. A.; Sloan, E. D.; Wu, D. T.; Sum, A. K. The Cages, Dynamics, and Structuring of Incipient Methane Clathrate Hydrates. *Phys. Chem. Chem. Phys.* **2011**, *13*, 19951.
- (12) Zhang, Z.; Kusalik, P. G.; Wu, N.; Liu, C.; Zhang, Y. Molecular Simulation Study on the Stability of Methane Hydrate Confined in Slit-Shaped Pores. *Energy* **2022**, *257*, 124738.
- (13) Walsh, M. R.; Beckham, G. T.; Koh, C. A.; Sloan, E. D.; Wu, D. T.; Sum, A. K. Methane Hydrate Nucleation Rates from Molecular Dynamics Simulations: Effects of Aqueous Methane Concentration, Interfacial Curvature, and System Size. *J. Phys. Chem. C* **2011**, *115*, 21241–21248.
- (14) Jacobson, L. C.; Molinero, V. Can Amorphous Nuclei Grow Crystalline Clathrates? The Size and Crystallinity of Critical Clathrate Nuclei. *J. Am. Chem. Soc.* **2011**, *133*, 6458–6463.
- (15) Sarupria, S.; Debenedetti, G. P. Homogeneous Nucleation of Methane Hydrate in Microsecond Molecular Dynamics Simulations. *J. Phys. Chem. Lett.* **2012**, *3*, 2942–2947.
- (16) Knott, B. C.; Molinero, V.; Doherty, M. F.; Peters, B. Homogeneous Nucleation of Methane Hydrates: Unrealistic under Realistic Conditions. *J. Am. Chem. Soc.* **2012**, *134*, 19544–19547.
- (17) Zhang, Z.; Walsh, M. R.; Guo, G. J. Microcanonical Molecular Simulations of Methane Hydrate Nucleation and Growth: Evidence That Direct Nucleation to SI Hydrate Is Among the Multiple Nucleation Pathways. *Phys. Chem. Chem. Phys.* **2015**, *17*, 8870–8876.
- (18) Ji, H.; Wu, G.; Zi, M.; Chen, D. Microsecond Molecular Dynamics Simulation of Methane Hydrate Formation in Humic-Acid-Amended Sodium Montmorillonite. *Energy Fuel.* **2016**, *30*, 7206–7213.
- (19) Zhang, Z.; Guo, G.-J. The Effects of Ice on Methane Hydrate Nucleation: A Microcanonical Molecular Dynamics Study. *Phys. Chem. Chem. Phys.* **2017**, *19*, 19496–19505.
- (20) Zhang, Z.; Liu, C.-J.; Walsh, M. R.; Guo, G.-J. Effects of Ensembles on Methane Hydrate Nucleation Kinetics. *Phys. Chem. Chem. Phys.* **2016**, *18*, 15602–15608.
- (21) Liao, Q.; Shi, B.; Li, S.; Song, S.; Chen, Y.; Zhang, J.; Yao, H.; Li, Q.; Gong, J. Molecular Dynamics Simulation of the Effect of Wax Molecules on Methane Hydrate Formation. *Fuel* **2021**, *297*, 120778.
- (22) Zi, M.; Wu, G.; Li, L.; Chen, D. Molecular Dynamics Simulations of Methane Hydrate Formation in Model Water-In-Oil Emulsion Containing Asphaltenes. *J. Phys. Chem. C* **2018**, *122*, 23299–23306.
- (23) Vatamanu, J.; Kusalik, P. G. Molecular Insights into the Heterogeneous Crystal Growth of SI Methane Hydrate. *J. Phys. Chem. B* **2006**, *110*, 15896–15904.
- (24) Hall, K. W.; Zhang, Z.; Burnham, C. J.; Guo, G.-J.; Carpendale, S.; English, N. J.; Kusalik, P. G. Does Local Structure Bias How a Crystal Nucleus Evolves? *J. Phys. Chem. Lett.* **2018**, *9*, 6991–6998.
- (25) Hall, K. W.; Zhang, Z.; Kusalik, P. G. Unraveling Mixed Hydrate Formation: Microscopic Insights into Early Stage Behavior. *J. Phys. Chem. B* **2016**, *120*, 13218–13223.
- (26) Wang, L.; Hall, K.; Zhang, Z.; Kusalik, G. P. Mixed Hydrate Nucleation: Molecular Mechanisms and Cage Structures. *J. Phys. Chem. B* **2022**, *126*, 7015–7026.
- (27) Liang, S.; Kusalik, P. G. Exploring nucleation of H<sub>2</sub>S hydrates. *Chem. Sci.* **2011**, *2*, 1286–1292.
- (28) Arjun; Berendsen, T. A.; Bolhuis, P. G. Unbiased Atomistic Insight in the Competing Nucleation Mechanisms of Methane Hydrates. *Proc. Natl. Acad. Sci. U.S.A.* **2019**, *116*, 19305–19310.
- (29) Jin, D.; Coasne, B. Reduced Phase Stability and Faster Formation/Dissociation Kinetics in Confined Methane Hydrate. *Proc. Natl. Acad. Sci. U.S.A.* **2021**, *118*, No. e2024025118.
- (30) Zhang, Z.; Kusalik, P. G.; Guo, G.-J. Bridging Solution Properties to Gas Hydrate Nucleation Through Guest Dynamics. *Phys. Chem. Chem. Phys.* **2018**, *20*, 24535–24538.
- (31) Ghaani, M. R.; Allen, C. C. R.; Skvortsov, T.; English, J. N. Engineering Peptides to Catalyze and Control Stabilization of Gas Hydrates: Learning From Nature. *J. Phys. Chem. Lett.* **2020**, *11*, 5068–5075.
- (32) He, Z.; Zhang, K.; Jiang, J. Formation of CH<sub>4</sub> Hydrate in a Mesoporous Metal-Organic Framework MIL-101: Mechanistic Insights from Microsecond Molecular Dynamics Simulations. *J. Phys. Chem. Lett.* **2019**, *10*, 7002–7008.
- (33) Cox, S. J.; Taylor, D. J. F.; Youngs, T. G. A.; Soper, A. K.; Totton, T. S.; Chapman, R. G.; Arjmandi, M.; Hodges, M. G.; Skipper, N. T.; Michaelides, A. Formation of Methane Hydrate in the Presence of Natural and Synthetic Nanoparticles. *J. Am. Chem. Soc.* **2018**, *140*, 3277–3284.
- (34) Min, J.; Kang, D. W.; Lee, W.; Lee, J. W. Molecular Dynamics Simulations of Hydrophobic Nanoparticle Effects on Gas Hydrate Formation. *J. Phys. Chem. C* **2020**, *124*, 4162–4171.
- (35) Liang, S.; Kusalik, P. G. Explorations of Gas Hydrate Crystal Growth by Molecular Simulations. *Chem. Phys. Lett.* **2010**, *494*, 123–133.
- (36) Turner, D. J. *Clathrate Hydrate Formation in Water-in-Oil Dispersions*. Colorado School of Mines; Arthur Lakes Library, 2005.
- (37) Zhang, J.; Li, C.; Shi, L.; Xia, X.; Yang, F.; Sun, G. The Formation and Aggregation of Hydrate in W/O Emulsion Containing Different Compositions: A Review. *Chem. Eng. J.* **2022**, *445*, 136800.
- (38) Zhang, X.; Gong, J.; Yang, X.; Slupe, B.; Jin, J.; Wu, N.; Sum, K. A. Functionalized Nanoparticles for the Dispersion of Gas Hydrates in Slurry Flow. *ACS Omega* **2019**, *4*, 13496–13508.
- (39) Zhang, D.; Huang, Q.; Wang, W.; Li, H.; Zheng, H.; Li, R.; Li, W.; Kong, W. Effects of waxes and asphaltenes on CO<sub>2</sub> hydrate nucleation and decomposition in oil-dominated systems. *J. Nat. Gas Sci. Eng.* **2021**, *88*, 103799.
- (40) Stoporev, A. S.; Semenov, A. P.; Medvedev, V. I.; Mendgaziev, R. I.; Istomin, V. A.; Sergeeva, D. V.; Manakov, A. Y.; Vinokurov, V. A. Formation and agglomeration of gas hydrates in gas - organic liquid - water systems in a stirred reactor: Role of resins/asphaltenes/surfactants. *J. Pet. Sci. Eng.* **2019**, *176*, 952–961.
- (41) Song, G.; Ning, Y.; Guo, P.; Li, Y.; Wang, W. Investigation on Hydrate Growth at the Oil-Water Interface: In the Presence of Wax and Surfactant. *Langmuir* **2021**, *37*, 6838–6845.
- (42) Zheng, H.; Huang, Q.; Wang, W.; Long, Z.; Kusalik, P. G. Induction Time of Hydrate Formation in Water-in-Oil Emulsions. *Ind. Eng. Chem. Res.* **2017**, *56*, 8330–8339.
- (43) Stoporev, A. S.; Manakov, A. Y.; Altunina, L. K.; Strelets, L. A.; Kosyakov, V. I. Nucleation Rates of Methane Hydrate from Water in Oil Emulsions. *Can. J. Chem.* **2015**, *93*, 882–887.
- (44) Stoporev, A. S.; Ogienko, A. G.; Sizikov, A. A.; Semenov, A. P.; Kopitsyn, D. S.; Vinokurov, V. A.; Svarovskaya, L. I.; Altunina, L. K.; Manakov, A. Y. Unexpected Formation of sII Methane Hydrate in Some Water-in-Oil Emulsions: Different Reasons for the Same Phenomenon. *J. Nat. Gas Sci. Eng.* **2018**, *60*, 284–293.
- (45) Sagidullin, A. K.; Stoporev, A. S.; Manakov, A. Y. Effect of Temperature on the Rate of Methane Hydrate Nucleation in Water-in-Crude Oil Emulsion. *Energy Fuels* **2019**, *33*, 3155–3161.
- (46) Stoporev, A. S.; Yu Manakov, A.; Manakov, A. Time-Dependent Nucleation of Methane Hydrate in a Water-in-Oil Emulsion: Effect of Water Redistribution. *Mendeleev Commun.* **2022**, *32*, 414–416.
- (47) Zhang, D.; Huang, Q.; Li, R.; Wang, W.; Zhu, X.; Li, H.; Wang, Y. Effects of Waxes on Hydrate Behaviors in Water-in-Oil Emulsions Containing Asphaltenes. *Chem. Eng. Sci.* **2021**, *244*, 116831.

- (48) Yegya Raman, A.; Aichele, P. C. Effect of Particle Hydrophobicity on Hydrate Formation in Water-in-Oil Emulsions in the Presence of Wax. *Energy Fuels* **2017**, *31*, 4817–4825.
- (49) Ning, Y.; Li, Y.; Song, G.; Wang, W.; Liu, X.; Liu, Z.; Zhang, J. Investigation on Hydrate Formation and Growth Characteristics in Dissolved Asphaltene-Containing Water-In-Oil Emulsion. *Langmuir* **2021**, *37*, 11072–11083.
- (50) Aichele, C. P.; Chapman, W. G.; Rhyne, L. D.; House, H. J.; Montesi, A.; Creek, L. J.; House, W. Nuclear Magnetic Resonance Analysis of Methane Hydrate Formation in Water-in-Oil Emulsions. *Energy Fuels* **2009**, *23*, 835–841.
- (51) Haber, A.; Akhafash, M.; Loh, C. K.; Aman, Z. M.; Fridjonsson, E. O.; May, E. F.; Johns, M. L. Hydrate Shell Growth Measured Using NMR. *Langmuir* **2015**, *31*, 8786–8794.
- (52) Song, G.; Ning, Y.; Li, Y.; Wang, W. Investigation on hydrate growth at the oil-water interface: In the presence of asphaltene. *Chin. J. Chem. Eng.* **2022**, *45*, 211–218.
- (53) Wang, W.; Huang, Q.; Zheng, H.; Wang, Q.; Zhang, D.; Cheng, X.; Li, R. Effect of Wax on Hydrate Formation in Water-in-Oil Emulsions. *J. Dispersion Sci. Technol.* **2020**, *41*, 1821–1830.
- (54) Zhang, D.; Huang, Q.; Li, R.; Li, H.; Wang, W.; Zheng, H.; Zhu, X.; Zhang, X. Nucleation and Growth of Gas Hydrates in Emulsions of Water in Asphaltene-Containing Oils. *Energy Fuels* **2021**, *35*, 5853–5866.
- (55) Moudrakovski, I. L.; McLaurin, G. E.; Ratcliffe, C. I.; Ripmeester, A. Methane and Carbon Dioxide Hydrate Formation in Water Droplets: Spatially Resolved Measurements from Magnetic Resonance Microimaging. *J. Phys. Chem. B* **2004**, *108*, 17591–17595.
- (56) Park, T.; Lee, J. Y.; Kwon, T. H. Effect of Pore Size Distribution on Dissociation Temperature Depression and Phase Boundary Shift of Gas Hydrate in Various Fine-Grained Sediments. *Energy Fuels* **2018**, *32*, 5321–5330.
- (57) Hsu, W.-H.; Hwang, I.-S. Investigating States of Gas in Water Encapsulated between Graphene Layers. *Chem. Sci.* **2021**, *12*, 2635–2645.
- (58) Hess, B.; Kutzner, C.; van der Spoel, D.; Lindahl, E. GROMACS 4: Algorithms for Highly Efficient, Load-Balanced, and Scalable Molecular Simulation. *J. Chem. Theory Comput.* **2008**, *4*, 435–447.
- (59) Brooks, C. L. Computer Simulation of Liquids. *J. Solution Chem.* **1989**, *18*, 99.
- (60) Míguez, J. M.; Conde, M. M.; Torré, J.-P. P.; Blas, F. J.; Piñeiro, M. M.; Vega, C. Molecular dynamics simulation of CO<sub>2</sub>hydrates: Prediction of three phase coexistence line. *J. Chem. Phys.* **2015**, *142*, 124505.
- (61) Costandy, J.; Michalis, V. K.; Tsimpanogiannis, I. N.; Stubos, A. K.; Economou, I. G. The Role of Intermolecular Interactions in the Prediction of the Phase Equilibria of Carbon Dioxide Hydrates. *J. Chem. Phys.* **2015**, *143*, 094506.
- (62) Essmann, U.; Perera, L.; Berkowitz, M. L.; Darden, T.; Lee, H.; Pedersen, L. G. A Smooth Particle Mesh Ewald Method. *J. Chem. Phys.* **1995**, *103*, 8577–8593.
- (63) Abascal, J. L. F.; Sanz, E.; García Fernández, R.; Vega, C. A Potential Model for the Study of Ices and Amorphous Water: TIP4P/Ice. *J. Chem. Phys.* **2005**, *122*, 234511.
- (64) Forester, T. R.; McDonald, I. R.; Klein, M. L. Intermolecular Potentials and the Properties of Liquid and Solid Hydrogen Sulphide. *Chem. Phys.* **1989**, *129*, 225–234.
- (65) Grabowska, J.; Blazquez, S.; Sanz, E.; Zerón, I. M.; Algaba, J.; Manuel Míguez, J.; Blas, F. J.; Vega, C. Solubility of Methane in Water: Some Useful Results for Hydrate Nucleation. *J. Phys. Chem. B* **2022**, *126*, 8553–8570.
- (66) Walsh, M. R.; Koh, C. A.; Sloan, E. D.; Sum, A. K.; Wu, D. T. Microsecond Simulations of Spontaneous Methane Hydrate Nucleation and Growth. *Science* **80** *2009*, *326*, 1095–1098.
- (67) Lu, Y.; Lv, X.; Li, Q.; Yang, L.; Zhang, L.; Zhao, J.; Song, Y. Molecular behavior of hybrid gas hydrate nucleation: separation of soluble H<sub>2</sub>S from mixed gas. *Phys. Chem. Chem. Phys.* **2022**, *24*, 9509–9520.
- (68) Liang, S.; Rozmanov, D.; Kusalik, P. G. Crystal Growth Simulations of Methane Hydrates in the Presence of Silica Surfaces. *Phys. Chem. Chem. Phys.* **2011**, *13*, 19856–19864.
- (69) Zhang, Z.; Guo, G.-J.; Wu, N.; Kusalik, P. G. Molecular Insights into Guest and Composition Dependence of Mixed Hydrate Nucleation. *J. Phys. Chem. C* **2020**, *124*, 25078–25086.
- (70) Jiménez-Angeles, F.; Firoozabadi, A. Enhanced Hydrate Nucleation Near the Limit of Stability. *J. Phys. Chem. C* **2015**, *119*, 8798–8804.
- (71) Liang, S.; Kusalik, P. G. Nucleation of Gas Hydrates within Constant Energy Systems. *J. Phys. Chem. B* **2013**, *117*, 1403–1410.
- (72) Martyna, G. J.; Klein, M. L.; Tuckerman, M. Nosé-Hoover chains: The canonical ensemble via continuous dynamics. *J. Chem. Phys.* **1992**, *97*, 2635–2643.
- (73) Parrinello, M.; Rahman, A. Polymorphic Transitions in Single Crystals: A New Molecular Dynamics Method. *J. Appl. Phys.* **1981**, *52*, 7182–7190.
- (74) Orabi, E. A.; Lamoureux, G. Simulation of Liquid and Supercritical Hydrogen Sulfide and of Alkali Ions in the Pure and Aqueous Liquid. *J. Chem. Theory Comput.* **2014**, *10*, 3221–3235.
- (75) Eggimann, B. L.; Sun, Y.; DeJaco, R. F.; Singh, R.; Ahsan, M.; Josephson, T. R.; Ilja Siepmann, J. Assessing the Quality of Molecular Simulations for Vapor-Liquid Equilibria: An Analysis of the TraPPE Database. *J. Chem. Eng. Data* **2019**, *65*, 1330–1344.
- (76) Potoff, J. J.; Siepmann, J. I. Vapor-Liquid Equilibria of Mixtures Containing Alkanes, Carbon Dioxide, and Nitrogen. *AIChE J.* **2001**, *47*, 1676–1682.
- (77) Martin, M. G.; Siepmann, J. Transferable Potentials for Phase Equilibria. 1. United-Atom Description of n-Alkanes. *J. Phys. Chem. B* **1998**, *102*, 2569–2577.
- (78) Jorgensen, W. L.; Madura, J. D.; Swenson, C. J. Optimized Intermolecular Potential Functions for Liquid Hydrocarbons. *J. Am. Chem. Soc.* **1984**, *106*, 6638–6646.
- (79) Rodger, P. M.; Forester, T. R.; Smith, W. Simulations of the Methane Hydrate/Methane Gas Interface near Hydrate Forming Conditions. *Fluid Phase Equilib.* **1996**, *116*, 326–332.
- (80) Moon, C.; Hawtin, R. W.; Rodger, P. M. Nucleation and Control of Clathrate Hydrates: Insights from Simulation. *Faraday Discuss.* **2007**, *136*, 367–382.
- (81) Guo, G.-J.; Zhang, Y.-G.; Liu, C.-J.; Li, K.-H. Using the Face-Saturated Incomplete Cage Analysis to Quantify the Cage Compositions and Cage Linking Structures of Amorphous Phase Hydrates. *Phys. Chem. Chem. Phys.* **2011**, *13*, 12048.
- (82) He, Z.; Linga, P.; Jiang, J. What are the key factors governing the nucleation of CO<sub>2</sub> hydrate? *Phys. Chem. Chem. Phys.* **2017**, *19*, 15657–15661.
- (83) Wilson, D. T.; Barnes, B. C.; Wu, D. T.; Sum, A. K. Molecular Dynamics Simulations of the Formation of Ethane Clathrate Hydrates. *Fluid Phase Equilib.* **2016**, *413*, 229–234.
- (84) He, Z.; Gupta, K. M.; Linga, P.; Jiang, J. Molecular Insights into the Nucleation and Growth of CH<sub>4</sub> and CO<sub>2</sub> Mixed Hydrates from Microsecond Simulations. *J. Phys. Chem. C* **2016**, *120*, 25225–25236.
- (85) Hall, K. W.; Carpendale, S.; Kusalik, P. G. Evidence From Mixed Hydrate Nucleation for a Funnel Model of Crystallization. *Proc. Natl. Acad. Sci. U.S.A.* **2016**, *113*, 12041–12046.
- (86) Martínez, L.; Andrade, R.; Birgin, E. G.; Martínez, J. M. PACKMOL: A Package for Building Initial Configurations for Molecular Dynamics Simulations. *J. Comput. Chem.* **2009**, *30*, 2157–2164.
- (87) Humphrey, W.; Dalke, A.; Schulten, K. VMD: Visual Molecular Dynamics. *J. Mol. Graph.* **1996**, *14*, 33–38.
- (88) Sosso, G. C.; Chen, J.; Cox, S. J.; Fitzner, M.; Pedevilla, P.; Zen, A.; Michaelides, A. Crystal Nucleation in Liquids: Open Questions and Future Challenges in Molecular Dynamics Simulations. *Chem. Rev.* **2016**, *116*, 7078–7116.
- (89) Kashchiev, D.; Firoozabadi, A. Driving Force for Crystallization of Gas Hydrates. *J. Cryst. Growth* **2002**, *241*, 220–230.
- (90) Chapoy, A.; Mohammadi, A. H.; Tohidi, B.; Valtz, A.; Richon, D. Experimental Measurement and Phase Behavior Modeling of

Hydrogen Sulfide–Water Binary System. *Ind. Eng. Chem. Res.* **2005**, *44*, 7567–7574.

(91) Chapoy, A.; Mokraoui, S.; Valtz, A.; Richon, D.; Mohammadi, A. H.; Tohidi, B. Solubility measurement and modeling for the system propane–water from 277.62 to 368.16 K. *Fluid Phase Equilib.* **2004**, *226*, 213–220.

(92) Deroche, I.; Daou, T. J.; Picard, C.; Coasne, B. Reminiscent Capillarity in Subnanopores. *Nat. Commun.* **2019**, *10*, 4642.

(93) Mohr, S.; Pétuya, R.; Wyldé, J.; Sarria, J.; Purkayastha, N.; Ward, Z.; Bodnar, S.; Tsimpanogiannis, I. N. Size Dependence of the Dissociation Process of Spherical Hydrate Particles via Microsecond Molecular Dynamics Simulations. *Phys. Chem. Chem. Phys.* **2021**, *23*, 11180–11185.

(94) Johnston, J. C.; Molinero, V. Crystallization, Melting, and Structure of Water Nanoparticles at Atmospherically Relevant Temperatures. *J. Am. Chem. Soc.* **2012**, *134*, 6650–6659.

(95) Zhang, Z.; Kusalik, P. G.; Guo, G.-J.; Ning, F.; Wu, N. Insight on the Stability of Polycrystalline Natural Gas Hydrates by Molecular Dynamics Simulations. *Fuel* **2021**, *289*, 119946.

(96) Petrov, O.; Furó, I. Curvature-Dependent Metastability of the Solid Phase and the Freezing–Melting Hysteresis in Pores. *Phys. Rev. E* **2006**, *73*, 11608.

(97) Christenson, H. K. Confinement Effects on Freezing and Melting. *J. Phys. Condens. Matter* **2001**, *13*, R95–R133.

(98) Adeniyi, K. I.; Deering, C. E.; Nagabushana, G. P.; Marriott, R. A. Hydrogen Sulfide Hydrate Dissociation in the Presence of Liquid Water. *Ind. Eng. Chem. Res.* **2018**, *57*, 15579–15585.

(99) Anderson, R.; Llamedo, M.; Tohidi, B.; Burgass, R. W. Experimental Measurement of Methane and Carbon Dioxide Clathrate Hydrate Equilibria in Mesoporous Silica. *J. Phys. Chem. B* **2003**, *107*, 3507–3514.

(100) Li, L.; Zhong, J.; Yan, Y.; Zhang, J.; Xu, J.; Francisco, J. S.; Zeng, X. C. Unraveling Nucleation Pathway in Methane Clathrate Formation. *Proc. Natl. Acad. Sci. U.S.A.* **2020**, *117*, 24701–24708.

(101) Naeiji, P.; Woo, T. K.; Alavi, S.; Ohmura, R. Molecular Dynamics Simulations of Interfacial Properties of the CO<sub>2</sub>-Water and CO<sub>2</sub>-CH<sub>4</sub>-Water Systems. *J. Chem. Phys.* **2020**, *153*, 044701.

(102) Liang, S.; Hall, K. W.; Laaksonen, A.; Zhang, Z.; Kusalik, P. G. Characterizing Key Features in the Formation of Ice and Gas Hydrate Systems. *Philos. Trans. R. Soc., A* **2019**, *377*, 20180167.

(103) Majid, A. A. A.; Saidian, M.; Prasad, M.; Koh, C. A. Measurement of the Water Droplet Size in Water-in-Oil Emulsions Using Low Field Nuclear Magnetic Resonance for Gas Hydrate Slurry Applications. *Can. J. Chem.* **2015**, *93*, 1007–1013.

(104) Vatamanu, J.; Kusalik, P. G. Unusual Crystalline and Polycrystalline Structures in Methane Hydrates. *J. Am. Chem. Soc.* **2006**, *128*, 15588–15589.

(105) Jacobson, L. C.; Hujo, W.; Molinero, V. Thermodynamic Stability and Growth of Guest-Free Clathrate Hydrates: A Low-Density Crystal Phase of Water. *J. Phys. Chem. B* **2009**, *113*, 10298–10307.

(106) Gao, S. Investigation of Interactions between Gas Hydrates and Several Other Flow Assurance Elements. *Energy Fuels* **2008**, *22*, 3150–3153.